HHS Public Access

Author manuscript

Phys Med Biol. Author manuscript; available in PMC 2022 June 02.

Published in final edited form as:

Phys Med Biol. ; 66(11): . doi:10.1088/1361-6560/ac01f1.

Optical scatter imaging of resected breast tumor structures matches the patterns of micro-computed tomography

Samuel S Streeter[1,*], **Benjamin W Maloney**[1], **Rebecca A Zuurbier**[2,3], **Wendy A Wells**[2,3], **Richard J Barth**[2,3], **Keith D Paulsen**[1,3], **Brian W Pogue**[1,3,*]

[1]Thayer School of Engineering, Dartmouth College, Hanover, NH03755, United States of America

[2]Departments of Radiology (RAZ), Pathology and Laboratory Medicine (WAW), and Surgery (RJB), Dartmouth-Hitchcock Medical Center, Lebanon NH03756, United States of America

[3]Norris Cotton Cancer Center, Dartmouth-Hitchcock Medical Center, Lebanon NH03756, United States of America

Abstract

In patients undergoing breast-conserving surgery (BCS), the rate of re-excision procedures to remove residual tumor left behind after initial resection can be high. Projection radiography, and recently, volumetric x-ray imaging are used to assess margin adequacy, but x-ray imaging lacks contrast between healthy, abnormal benign, and malignant fibrous tissues important for surgical decision making. The purpose of this study was to compare micro-CT and optical scatter imagery of surgical breast specimens and to demonstrate enhanced contrast-to intra-tumoral morphologies and tumor boundary features revealed by optical scatter imaging. A total of 57 breast tumor slices from 57 patients were imaged *ex vivo* by spatially co-registered micro-CT and optical scatter scanning. Optical scatter exhibited greater similarity with micro-CT in 89% (51/57) of specimens versus diffuse white light (DWL) luminance using mutual information (mean ± standard deviation of 0.48 ± 0.21 versus 0.24 ± 0.12; $p < 0.001$) and in 81% (46/57) of specimens using the Sørensen–Dice coefficient (0.48 ± 0.21 versus 0.33 ± 0.18; $p < 0.001$). The coefficient of variation (CV) quantified the feature content in each image. Optical scatter exhibited the highest CV in every specimen (optical scatter: 0.70 ± 0.17; diffuse luminance: 0.24 ± 01; micro-CT: 0.15 ± 0.03 for micro-CT; $p < 0.001$). Optical scatter also exhibited the highest contrast ratios across representative tumor boundaries with adjacent healthy/benign fibrous tissues (1.5–3.7 for optical scatter; 1.0–1.1 for diffuse luminance; 1.0–1.1 for micro-CT). The two main findings from this study were: first, optical scatter contrast was in general similar to the radiological view of the tissue relative to DWL imaging; and second, optical scatter revealed additional features associated with fibrous tissue structures of similar radiodensity that may be relevant to diagnosis. The value of micro-CT lies in its rapid three-dimensional scanning of specimen morphology, and combined

[*]Authors to whom any correspondence should be addressed. Samuel.S.Streeter.TH@Dartmouth.edu and Brian.W.Pogue@Dartmouth.edu.

Ethical statement

All aspects of this study followed a protocol approved by the Institutional Review Board at Dartmouth and were in accordance with the 1964 Declaration of Helsinki and its later amendments. Written informed consent from patients involved in this study was waived by the Institutional Review Board at Dartmouth, because the study involved only de-identified tissue samples, presented no risk to involved patients, and did not alter the outcome of any patient's diagnosis or medical treatment in any way.

Supplementary material for this article is available online

with optical scatter imaging with sensitivity to fibrous surface tissues, may be an attractive solution for margin assessment during BCS.

Keywords

breast cancer; breast-conserving surgery; micro-CT; optical scatter imaging; spatial frequency domain imaging

1. Introduction

Breast-conserving surgery involves local excision of cancer with a surrounding margin of healthy tissue with the goal of resecting the disease completely while sparing healthy tissue and preserving the shape and appearance of the breast. Today, BCS in combination with radiation therapy is the most common treatment for *in situ* and early stage breast cancers (American Cancer Society 2019). Current practice in BCS relies on surgeon expertise, as palpation and visual inspection are primarily used to guide tumor excision. Projection radiography is used to determine margin adequacy intraoperatively, but margins normal to the imaging plane and features along peripheral margins may be poorly resolved and thus difficult to assess. The gold standard for BCS specimen margin assessment is histopathology, which is performed post-operatively and often completed several hours to days after the procedure. The rate of re-excision procedures to remove residual tumor is high in cancer patients undergoing initial BCS due to the limited intraoperative tools available. Approximately 20% of BCS patients require a second surgery due to incomplete initial excision (16%–33% depending on the medical center, cancer type, and surgeon) (Fleming et al 2004, Balch et al 2005, Lovrics et al 2010, McCahill et al 2012, Kaczmarski et al 2019). Consequences of re-excision include increased potential for surgery-related complications, less desirable cosmetic outcomes, delayed adjuvant therapy, and increased healthcare costs (Wazer et al 1992, Heil et al 2012, Moran et al 2014). Recent studies have explored the value of volumetric micro-computed tomography (micro-CT) (Tang et al 2016,McClatchy et al 2018, DiCorpo et al 2020) and tomosynthesis (Chagpar et al 2015, Park et al 2019, Partain et al 2020) for improving intraoperative BCS margin assessment. These technologies overcome the dimensional limitation inherent to projection imaging and provide rapid sensing of the three-dimensional morphology of specimens. Nonetheless, x-ray imaging alone lacks contrast between normal, abnormal benign and malignant fibrous tissues that may be important for assessing breast tumor margins (Kopans 2006). Coupling volumetric x-ray imaging with other imaging modalities sensitive to fibrous tissue subtypes may be one attractive solution for margin assessment (Maloney et al 2018, McClatchy et al 2018, DiCorpo et al 2020).

Several imaging techniques have been proposed for improving BCS margin assessment, including compact magnetic resonance imaging (Papa et al 2016), diffuse reflectance spectroscopy (de Boer et al 2016), Raman spectroscopy (Wang et al 2016), fluorescence microscopy (Tongtong et al 2020), and photoacoustic microscopy (Wong et al 2017). A typical BCS resection will have a surface area that is 10 s of cm^2, roughly 45 cm^2 on average, based on a recent study (DiCorpo et al 2020). The relatively small field-of-view of

these imaging techniques (i.e. 100 s μm^2–1 cm^2) limits their potential to thoroughly analyze the surface of a BCS resection in a clinically relevant timeframe. Intraoperative pathological techniques, including frozen section pathology, touch smear, and imprint cytology, are used in some medical centers for BCS margin assessment, but these methods are known to be time- and resource-intensive (Butler-Henderson et al 2014).

In this study, BCS specimens were imaged using micro-CT and wide field-of-view (>100 cm^2) optical scatter imaging. The optical imaging method used is known as spatial frequency domain imaging, which involves illuminating the tissue with one-dimensional sinusoidal patterns of light and imaging the reflected light intensity. When the sinusoidal patterns are finer than the length scale of diffuse photon transport, the measured reflectance is dominated by sub-diffusely scattered photons, and the observed contrast is dominated by optical scatter (Krishnaswamy et al 2014). This form of optical scatter imaging provides rapid, non-contact, and wide field scanning of the top layer of tissue with increased sensitivity to tumor-associated, collagen-rich matrix structures (<1 mm depth sensitivity) (McClatchy et al 2016) and does not require any exogenous contrast agents. Diffuse white light (DWL) imaging, which is similar to the surgeon's view of the tissue in the operating room, and optical scatter imaging were compared directly to micro-CT for visualizing BCS specimens exhibiting 13 distinct tissue subtypes confirmed by histopathological analysis. The goal of the study was to investigate the potential synergy between micro-CT and optical scatter imaging for analyzing BCS tissues.

2. Methods

2.1. Study protocol

Multimodal micro-CT and optical scatter imaging of BCS specimens was performed at the Dartmouth-Hitchcock Medical Center (DHMC) in Lebanon, New Hampshire. The observational study was approved by the Institutional Review Board at Dartmouth for protection of human subjects, and all procedures followed the approved protocol. Procurement of tissue specimens involved patients undergoing consented and elective breast surgeries at DHMC. Specimen imaging occurred post-operatively during standard pathological processing using a validated multimodal imaging system (McClatchy et al 2017) and did not impact clinical workflow or subsequent tissue processing and diagnostic reporting. Each resected BCS tumor was 'bread-loafed,' or sliced into ~5 mm thick sections perpendicular to its long axis according to standard of care practices at DHMC. One representative slice from each tumor was selected by an experienced Pathologists' Assistant, positioned firmly between optically clear acrylic plates, and imaged *ex vivo* in the multimodal system, which was stationed in the specimen grossing laboratory. Each imaged specimen was de-identified and referenced only by a unique specimen accessioning number. The top surface of each imaged slice underwent standard of care specimen processing, sectioning, staining with hematoxylin and eosin, and microscopic analysis by a board-certified breast pathologist (WAW). Representative histologic glass slides corresponding to the imaged tissue underwent whole slide, high resolution digital imaging to confirm tissue subtype regions of interest (ROIs). These microscopic ROIs were co-registered to the wide field-of-view micro-CT and optical imagery.

2.2. Imaging system

Micro-CT scans were performed using an IVIS SpectrumCT system (PerkinElmer, Hopkington, MA) housing a cone-beam CT in a 'pancake' geometry and with settings reported in a previous BCS specimen study (McClatchy et al 2018). X-ray settings were 50 kVp and 1 mA with a 440 μm aluminum filter. The x-ray source-detector distance was fixed with a 50 μm focal spot size. A scan involved 360° rotation of the specimen with a 100 ms exposure every 0.5° (720 total projections). A scan volume of 12 × 12 × 3 cm^3 was reconstructed with 150 μm^3 voxels (~4 min acquisition and reconstruction). The x-ray detector (3072 × 864 pixels) was binned by a factor of four (1024 × 216 pixels) to increase the signal-to-noise ratio and reduce total scan time. The optical imaging system consisted of the native SpectrumCT charged coupled device camera (Andor iKon, Andor Technologies Ltd, Belfast, UK) and a digital light projector (CEL5500 Fiber, Digital Light Innovations Inc., Austin, TX) retrofitted into the light-tight, fully shielded SpectrumCT imaging cabinet. Optical imaging involved acquisitions at seven wavelengths (λ = 490–800 nm, 15 nm bandwidth) and seven structured illumination frequencies (f_X = 0.00–1.37 mm^{-1}) produced by the digital light projector (~8 min acquisition and saving). The optical imaging field-of-view was ~13 cm × ~13 cm with a pixel size in the imaging plane of ~126 μm × ~126 μm. Additional information about the type of optical structured light imaging used in this study is available (see appendix 1 in supplementary material and a video demonstrating the optical imaging in multimedia S1 (available online at stacks.iop.org/PMB/66/115021/mmedia)). Each imaged specimen was positioned firmly between acrylic plates and was not moved or altered between micro-CT and optical image acquisition, allowing for spatial co-registration between the two modalities.

2.3. Image data and pre-processing

A total of 70 BCS tumor specimens were imaged using the study protocol. Previous studies analyzed only the optical image data from these 70 specimens, demonstrating statistical differentiation between healthy, abnormal benign, and malignant tissue subtypes using either optical property quantification (Maloney et al 2019) or reflectance textural information (Streeter et al 2019). Recently, the top tissue slice from each volumetric micro-CT scan (i.e. the tissue surface imaged optically) was extracted, rescaled, and spatially co-registered with the optical data of the same specimen using rigid transformations. The present study is the first quantitative analysis of the micro-CT data in the form of image similarity and quality relative to the co-registered optical images.

All optical images were converted to calibrated reflectance maps using a previously described normalization routine (McClatchy et al 2017) and were then median filtered using a 3 × 3 pixel kernel. All micro-CT slice images were extracted from volumetric scans calibrated to 50 kVp linear attenuation coefficient values (in units of cm^{-1}). No additional image pre-processing (e.g. histogram stretching) was performed on any image data prior to quantitative image analysis. Additional details about co-registration of the high resolution histology images to the wide field-of-view micro-CT and the optical images are available (appendix 2 in supplementary material and supplemental figure S1).

True color, DWL images of each specimen were reconstructed from planar illumination (f_X = 0.00 mm^{-1}) imagery at five wavelengths in the visible spectrum (λ = 490, 550, 650, 700 nm) using 1931 International Commission on Illumination color space tristimulus values (Smith and Guild 1931) and a previously described process (McClatchy et al 2017). These true color reconstructions represented how each tissue specimen would appear to the naked eye (e.g. to the surgeon in the operating room). Optical scatter color reconstructions were created by the same method, except using only the highest spatial frequency illumination data (f_X = 1.37 mm^{-1}). Optical scatter color reconstructions were not used in the image analysis in this study but were included for qualitative inspection. For the image analysis, true color DWL images were converted to grayscale intensity (i.e. luminance), and optical scatter images were derived from the shortest optical wavelength (λ = 490 nm) and highest spatial frequency pattern (f_X = 1.37 mm^{-1}). This created three grayscale (i.e. single channel) image types to be quantitatively compared: DWL luminance, monochromatic 490 nm optical scatter, and micro-CT.

Of 70 imaged specimens, five were excluded due to inconsistent micro-CT scan settings, six were excluded due to ambiguous histology co-registrations, one was excluded due to neo-adjuvant chemotherapy treatment, and one was excluded due to a small cross-sectional area (<2 cm^2). Thus, 57 specimens were further analyzed. Table 1 summarizes the 57 imaged specimens by primary tissue subtype diagnosis. Each specimen contained one or more tissue subtypes confirmed by microscopic histopathological analysis. Some specimens contained multiple benign and/or malignant subtypes with normal adipose tissue and/or connective tissue components.

2.4. Image analysis

Three forms of image analysis were performed in this study. First, mutual information (MI) and the Sørensen-Dice (Dice) coefficient quantified wide field similarity between micro-CT and optical images of all n = 57 specimens. MI was used as a pixel-level intensity distribution similarity metric, as it is insensitive to spatial relationships between pixels (Pluim et al 2003). The Dice coefficient based on an isodata binary thresholding algorithm (Ridler and Calvard 1978) compared high-contrast, two-dimensional structures in the optical and micro-CT images. DWL luminance versus micro-CT provided a baseline similarity measurement (i.e. an approximation of how the naked eye view relates to the radiological view of the tissue), and optical scatter versus micro-CT similarity was compared to this baseline.

The second form of analysis involved the quantification of the coefficient of variation (CV) for all n = 57 wide field specimen images. CV was defined as the ratio of the standard deviation of tissue pixel values divided by the mean value of tissue pixel values. CV provided a standardized measure of dispersion about the mean image pixel intensity and quantified the relative amount of feature content in each image (i.e. the image quality). An image with high CV was interpreted as having relatively more feature content, and vice versa.

The third form of analysis focused on targeted (i.e. 1.5 cm × 1.5 cm or 2 cm × 2 cm) regions in the micro-CT and optical imagery. CV was quantified within malignant tumor-bearing

sections and sections containing malignant tissue boundaries with adjacent healthy/benign fibrous tissue to quantify intra-tumoral and tumor boundary feature content, respectively. The tumor boundary contrast ratio (TBCR) was defined as the ratio of intensities between a malignant tissue region and adjacent healthy/benign fibrous tissue region (each being a 2 mm diameter circular sample of intensity). The TBCR was defined with the brighter and darker regions set to the numerator and denominator, respectively (thus, TBCR $\geqslant 1$ by definition; the numerator and denominator were set irrespective of malignancy). The TBCR quantified the malignant versus healthy/benign tissue boundary contrast achieved by each image type. TBCR was used instead of a conventional contrast-to-noise ratio (CNR, defined as the difference in intensity between the malignant and non-malignant regions divided by the standard deviation of the background), because sensitivity to tumor and fibrous tissue heterogeneity would be penalized by the quantification of CNR.

For comparing results from all $n = 57$ specimens, differences in MI, Dice coefficient, and CV were evaluated statistically using nonparametric Mann–Whitney U tests. A p-value of <0.05 was considered statistically significant. All image and statistical analyses were performed using Matlab (v2020a, Mathworks, Inc., Natick, MA). Additional information about the image analysis performed in this study is available (appendix 3 in supplementary material and supplemental figures S2–S5).

3. Results

Wide field-of-view images from representative invasive ductal carcinoma (IDCa) and invasive lobular carcinoma (ILCa) specimens are shown in figures 1 and 2, respectively. In these figures, true color DWL images appear in the leftmost column, followed by DWL luminance, optical scatter color reconstructions, monochromatic 490 nm optical scatter images, and spatially co-registered micro-CT slices in the remaining four columns.

Wide field-of-view micro-CT and optical image similarity analysis is summarized in figures 3(A)–(D). In figure 3(A), optical scatter and DWL luminance exhibited similar MI to micro-CT for healthy/benign tissue specimens (p-value = 0.11). Optical scatter exhibited greater MI with micro-CT than DWL luminance for IDCa specimens (p-value < 0.001) and greater MI with micro-CT than DWL luminance for ILCa specimens (p-value = 0.009). In figure 3(C), optical scatter and DWL luminance exhibited similar Dice coefficients with micro-CT for healthy/benign tissue specimens (p-value = 0.37). Optical scatter exhibited greater Dice coefficients with micro-CT than DWL luminance for IDCa specimens (p-value < 0.001) and similar Dice coefficients with micro-CT for ILCa specimens (p-value = 0.08). When specimens were analyzed as a single group, optical scatter images exhibited greater similarity with co-registered micro-CT slices in 89% (51/57) of specimens using MI (figure 3(B); mean ± standard deviation of 0.48 ± 0.21 versus 0.24 ± 0.12; $p < 0.001$) and in 81% (46/57) of specimens using the Dice coefficient (figure 3(D); mean ± standard deviation of 0.48 ± 0.21 versus 0.33 ± 0.18; $p < 0.001$).

CV values quantified from the wide field-of-view images effectively separated the three image types with statistical significance (figures 3(E) and (F)). In 100% (57/57) of specimens, optical scatter yielded the highest CV values, indicating that this image type

generated the greatest dispersion about the mean tissue pixel intensity compared to co-registered DWL luminance and micro-CT images.

Figure 4 shows close-ups of BCS specimen tumor-bearing sections. In the leftmost column, wide field-of-view, true color DWL specimen images show red ROIs that delineate malignant tissue confirmed by histopathology. Square regions shown in this column (white border, 1.5 cm × 1.5 cm) are magnified in the next three columns of each row to visually highlight differences between the optical and micro-CT images. Figure 5 presents tumor-bearing sections that contain malignant tissue boundaries with adjacent healthy/benign fibrous tissue. In the leftmost column, wide field-of-view, true color DWL specimen images show color-coded tissue subtype ROIs, and square regions (white border, 2 cm × 2 cm) containing malignant tissue boundaries are magnified in the next three columns of each row, again to highlight differences in the images.

Figure 6(A) summarizes image quality analysis performed on the 1.5 cm × 1.5 cm ROIs containing intra-tumoral structures shown in figure 4. For these $n = 4$ representative specimens, optical scatter exhibited the highest CV in every case (0.20–0.30 versus 0.04–0.09 for DWL luminance, 0.03–0.08 micro-CT). Figure 6(B) summarizes image quality analysis performed on 2.0 cm by 2.0 cm ROIs containing malignant boundaries with adjacent healthy or benign fibrous tissue. For these $n = 4$ representative specimens, optical scatter again exhibited the highest CV in every case (0.43–0.67 versus 0.13–0.31 for DWL luminance, 0.11–0.25 micro-CT), suggesting greater sensitivity to malignant tissue boundaries with adjacent fibrous tissue. Figure 6(C) reports TBCR values quantified from 2 mm diameter samples on either side of the tumor boundaries shown in figure 5 (solid colored dots in column 1). TBCR values for the $n = 4$ representative specimens in figure 5 were 1.5–3.7 for optical scatter, while the same samples yielded TBCR values of 1.0–1.1 for both DWL luminance and micro-CT.

4. Discussion

The purpose of this study was to directly compare micro-CT and optical scatter images of surgical breast specimens. In general, monochromatic 490 nm optical scatter and micro-CT exhibited similar contrast between epithelial and stromal features relative to backgrounds of low intensity adipose tissue. Figures 1 and 2 show this visually, and image analysis results in figures 3(A)–(D) corroborate this finding quantitatively using MI and Dice coefficient. Optical scatter and micro-CT had greater MI (p-value <0.001) and greater Dice coefficient (p-value <0.001)versus DWL luminance and micro-CT overall.

The fact that optical scatter relates to the radiological view of the tissue, despite having a distinct mechanism of contrast, is notable. X-ray contrast is based on attenuation resulting from both scattering and absorption events and is governed by the Beer–Lambert law, $N_{\text{out}}(E) = N_{\text{in}}(E)e^{-\int_0^l \mu(x, Z, A, \rho, E)dx}$, where N_{in} and N_{out} are the incident and exiting x-rays on either side of a tissue sample, respectively, E is the x-ray photon energy, and μ is the linear attenuation coefficient, which may depend on spatial position (x) in a tissue sample of certain thickness (l), and on the atomic number (Z), atomic mass (A), and density (ρ) of the tissue. X-ray contrast arises from differences in tissue μ, mainly

from changes in tissue density (e.g. $\rho_{\text{Adipose}} \approx 0.94$ g cm^{-3} versus $\rho_{\text{OtherSoftTissue}} \approx 1$ g cm^{-3} in BCS specimens) and from high atomic number material (e.g. $Z_{\text{calcium}} = 20$ in BCS specimen microcalcifications) (Bushberg et al 2012). Tissue density (i.e. electron density) differences primarily impact x-ray attenuation due to Compton scattering, which has the following proportionality: $\mu_{\text{Compton}} \propto \rho \frac{Z}{A}$. Atomic number differences, meanwhile, primarily impact x-ray attenuation due to the photoelectric effect, which has the following proportionality: $\mu_{\text{Photoelectric}} \propto \frac{Z^3}{E^3}$ (Bushberg et al 2012). X-ray imaging is less effective at detecting microscopic differences between healthy, abnormal benign, and malignant fibrous tissues, because these tissues have similar radiodensity (i.e. similar tissue density and effective atomic number) over the range of diagnostic x-ray energies (roughly 10–150 keV).

Optical scatter contrast is fundamentally tied to the length scale of index of refraction fluctuations in tissue relative the wavelength of incident light. Index of refraction fluctuations that are larger than the incident optical photon wavelength result in forward-dominant Mie scattering, while fluctuations that are smaller result in Rayleigh scattering with relatively more backscattering (McClatchy et al 2016). Collagen fibrils (10 s of nm in diameter) and striations (<100 nm in diameter) are key Rayleigh scattering components in breast tissue for optical wavelengths of light and thus contribute positive scatter contrast. In the context of breast cancer, optical scatter contrast depends on the proportion of connective tissue matrix versus epithelial tissue, with increased sensitivity to tumor-associated, collagen-rich matrix, as observed in the optical scatter images presented in this study (e.g. connective tissues in figure 5 IDCa, IG and IDCa, HG specimens). Meanwhile, adipose tissue vacuoles (>25 μm in diameter) and tightly packed sheets of epithelium characteristic of high grade IDCa with high nuclear density (nuclei diameters being ≈5 μm) result in Mie-type scattering with relatively less backscattering and thus lower reflectance (e.g. adipose tissue in figures 1 and 2; malignant tissue in the figure 5 IDCa, HG specimen).

MI and Dice coefficient values reported in this study also indicate micro-CT and optical scatter imaging have differences in image feature content. Results in figures 3(E) and (F) reinforce this point, showing significantly higher CV values for optical scatter images (p-value <0.001) relative to both DWL luminance and micro-CT. These relatively high CV values were in part due to the enhanced contrast that optical scatter has to intra-tumoral fibrous structures and tumor boundary features. Subsets of specimens containing either clear cross sections of malignant tissue (figure 4) or boundaries between malignant and non-malignant fibrous tissue (figure 5) underscore the potential value of optical scatter imaging in the context of imaging BCS specimen margins. CV values from within tumor-bearing ROIs and malignant tissue boundary ROIs were greatest for optical scatter relative to DWL luminance and micro-CT (figures 6(A) and (B)). When malignant tissue is adjacent to healthy and/or benign fibrous tissue, TBCR values were highest for optical scatter relative to DWL luminance and micro-CT as well (figure 6(C)). This result suggests that optical scatter may be able to leverage the known association between the growth and alignment of collagen structures and breast cancer for improving margin assessment (Conklin et al 2011, Cox and Erler 2014). Importantly, optical scatter contrast-to malignant tissue is not

necessarily positive (i.e. brighter) relative to surrounding tissues (e.g. all specimens shown in figure 5). Nonetheless, abrupt changes in optical scatter intensity and/or texture that correspond to malignancy boundaries or tumor-associated collagen structures may be of value for diagnostic interpretation of BCS specimen margins and for performing targeted shave biopsies to remove residual tumor during initial BCS procedures.

The image data in this study exemplify the highly heterogenous nature of breast cancer, both in terms of macroscale morphology and microscopic histological diagnosis, but sample sizes were too small to derive robust statistical differences based on individual tissue subtypes. Another study limitation is the fact that only BCS specimen slices were imaged, rather than the margins of intact BCS resections. Nevertheless, representative specimen slices offered the greatest diversity of healthy, abnormal benign, and malignant tissues to demonstrate differences in micro-CT and optical contrast. Ring artifacts were present in a subset of the micro-CT images due to failed detector pixels in the IVIS SpectrumCT system. Projection pattern artifacts in some optical images were also visible, appearing as fine scale, one-dimensional fluctuations in intensity. Specular reflection artifacts were also present in some optical images, appearing as localized spikes in intensity. Recent work demonstrated a new method of wide field-of-view optical imaging to isolate scatter contrast using a scanned laser line (Streeter et al 2020). The method provided an order of magnitude greater dynamic range than the optical structured light imaging method used here and will be investigated in future BCS specimen imaging studies. Micro-CT scanning benefits from being relatively insensitive to tissue thickness over length scales relevant to BCS specimens and impervious to irregular tissue surface geometries. In contrast, optical scatter imaging has only surface layer sensitivity, which is a benefit for providing spatially localized reflectance, but suffers from specular reflection and demodulation artifacts that arise from irregular tissue surfaces. This limitation necessitates the use of optically clear plates to create a flat, consistent tissue surface for wide field imaging. Future work will attempt to overcome this limitation of optical scatter imaging by leveraging stereovision imaging to filter specular reflections and enable imaging of irregular, three-dimensional tissue surfaces (Geng 2011). Finally, while this initial comparison study highlights the potential synergy of micro-CT combined with optical scatter imaging, future work will quantitatively measure the improvement in BCS specimen margin assessment using combined micro-CT and optical scatter imaging.

In this study, a total of 57 BCS tumor specimens exhibiting 13 pathology-confirmed tissue subtypes were imaged using spatially co-registered micro-CT and optical scatter imaging. The two main findings from this study were: first, optical scatter contrast was in general similar to the radiological view of the tissue relative to DWL luminance; and second, optical scatter revealed additional features associated with fibrous tissue structures of similar radiodensity that may be relevant to diagnosis. Volumetric x-ray imaging has clear value in its ability to rapidly scan the three-dimensional morphology of BCS specimens. Micro-CT also has sensitivity to microcalcifications, which are not visible in the optical images (e.g. ILCa specimen in figure 4), and are known to be related the histology of breast cancer lesions (Tse et al 2008). The inability of micro-CT to clearly differentiate fibrous tissues on BCS specimen margins may be addressed by coupling micro-CT with optical scatter imaging, which senses reflectance from only the superficial layer of tissue with contrast arising primarily from highly scattering, collagen-rich fibrous tissues. Future work

will focus on micro-CT specimen scanning complemented by co-registered optical scatter imaging to provide increased sensitivity to fibrous tissue subtypes and tumor structures and boundaries that may appear along BCS specimen margins.

5. Conclusions

BCS re-excision rates can be high due to incomplete initial resection of cancerous tissue. Improved intraoperative margin assessment could reduce the number of re-excision procedures and associated health and financial costs. Projection radiography is standard of care for intraoperative BCS specimen imaging, and volumetric x-ray scanning is emerging as a powerful intraoperative tool for sensing the three-dimensional morphology of BCS resections. However, x-ray imaging alone lacks contrast between tumor-associated collagen and healthy or otherwise benign collagen-rich tissues. The goal of this study was to investigate the potential synergy between micro-CT and optical scatter imaging for analyzing BCS tissues. Optical scatter contrast is similar to the radiological view of breast tissues in general but provides additional contrast between healthy, abnormal benign, and malignant fibrous tissues not readily differentiated by x-ray imaging. Optical scatter imaging with sensitivity to these fibrous tissue features has potential for improving intraoperative evaluation of margin adequacy during BCS procedures relative to x-ray-based imaging alone.

Supplementary Material

Refer to Web version on PubMed Central for supplementary material.

Acknowledgments

Study support came from the National Institutes of Health (R01CA192803). BWP, SSS, BWM, and KDP have a patent pending (US Application No.: 17/076,788) related to this study. RJB is Co-Founder and CMO of CairnSurgical, Inc. KDP is Co-Founder of CairnSurgical, Inc. BWP is President and Co-Founder of DoseOptics, LLC. Authors in their roles in the medical industry did not in any way impact this study. The authors thank Dr Brady Hunt, Research Scientist at Dartmouth College, for helpful discussions related to the study.

References

American Cancer Society 2019 Breast Cancer Facts and Figures 2019–2020 (Atlanta, GA: American Cancer Society, Inc.)

Balch GC, Mithani SK, Simpson JF and Kelley MC 2005 Accuracy of intraoperative gross examination of surgical margin status in women undergoing partial mastectomy for breast malignancy Am. Surg 71 22–7 [PubMed: 15757052]

Bushberg J, Seibert J, Leidholdt E and Boone J 2012 The Essential Physics in Medical Imaging (Philadelphia, PA: Lippincott Williams & Wilkins)

Butler-Henderson K, Lee AH, Price RI and Waring K 2014 Intraoperative assessment of margins in breast conserving therapy: a systematic review Breast Edinb. Scotl 23 112–9

Chagpar AB, Butler M, Killelea BK, Horowitz NR, Stavris K and Lannin DR 2015 Does three-dimensional intraoperative specimen imaging reduce the need for re-excision in breast cancer patients? A prospective cohort study Am. J. Surg 210 886–90 [PubMed: 26255230]

Conklin MW, Eickhoff JC, Riching KM, Pehlke CA, Eliceiri KW, Provenzano PP, Friedl A and Keely PJ 2011 Aligned collagen is a prognostic signature for survival in human breast carcinoma Am. J. Pathol 178 1221–32 [PubMed: 21356373]

Cox TR and Erler JT 2014 Molecular pathways: connecting fibrosis and solid tumor metastasis Clin. Cancer Res 20 3637–43 [PubMed: 25028505]

de Boer LL, Hendriks BHW, van Duijnhoven F, Peeters-Baas M-JTFDV, Van de Vijver K, Loo CE, Jóźwiak K, Sterenborg HJCM and Ruers TJM 2016 Using DRS during breast conserving surgery: identifying robust optical parameters and influence of inter-patient variation Biomed. Opt. Express 7 5188–200 [PubMed: 28018735]

DiCorpo D, Tiwari A, Tang R, Griffin M, Aftreth O, Bautista P, Hughes K, Gershenfeld N and Michaelson J 2020 The role of Micro-CT in imaging breast cancer specimens Breast Cancer Res. Treat 180 343–57 [PubMed: 32020431]

Fleming FJ, Hill ADK, Mc Dermott EW, O'Doherty A, O'Higgins NJ and Quinn CM 2004 Intraoperative margin assessment and re-excision rate in breast conserving surgery Eur. J. Surg. Oncol 30 233–7 [PubMed: 15028301]

Geng J 2011 Structured-light 3D surface imaging: a tutorial Adv. Opt. Photonics 3 128–60

Heil J, Breitkreuz K, Golatta M, Czink E, Dahlkamp J, Rom J, Schuetz F, Blumenstein M, Rauch G and Sohn C 2012 Do reexcisions impair aesthetic outcome in breast conservation surgery? Exploratory analysis of a prospective cohort study Ann. Surg. Oncol 19 541–7 [PubMed: 21761099]

KaczMarski K, Wang P, Gilmore R, Overton HN, Euhus DM, Jacobs LK, Habibi M, Camp M, Weiss MJ and Makary MA 2019 Surgeon re-excision rates after breast-conserving surgery: a measure of low-value care J. Am. Coll. Surg 228 504–512.e2 [PubMed: 30703538]

Kopans D 2006 Breast Imaging (Philadelphia, PA: Lippincott Williams &Wilkins)

Krishnaswamy V, Elliott JT, McClatchy DM 3rd, Barth RJJ, Wells WA, Pogue BW and Paulsen KD 2014 Structured light scatteroscopy Proc. SPIE 19 070504

Lovrics PJ, Cornacchi SD, Farrokhyar F, Garnett A, Chen V, Franic S and Simunovic M 2010 Technical factors, surgeon case volume and positive margin rates after breast conservation surgery for early-stage breast cancer Can. J. Surg 53 305–12 [PubMed: 20858374]

Maloney BW, McClatchy DM, Pogue BW, Paulsen KD, Wells WA and Barth RJ 2018 Review of methods for intraoperative margin detection for breast conserving surgery Proc. SPIE 23 100901

Maloney BW, Streeter SS, McClatchy DM, Pogue BW, Rizzo EJ, Wells WA and Paulsen KD 2019 Structured light imaging for breast-conserving surgery: I. Optical scatter and color analysis Proc. SPIE 24 096002

McCahill LE, Single RM, Aiello Bowles EJ, Feigelson HS, James TA, Barney T, Engel JM and Onitilo AA 2012 Variability in reexcision following breast conservation surgery JAMA 307 467–75 [PubMed: 22298678]

McClatchy DM, Rizzo EJ, Meganck J, Kempner J, Vicory J, Wells WA, Paulsen KD and Pogue BW 2017 Calibration and analysis of a multimodal micro-CT and structured light imaging system for the evaluation of excised breast tissue Phys. Med. Biol 62 8983–9000 [PubMed: 29048330]

McClatchy DM, Rizzo EJ, Wells WA, Cheney PP, Hwang JC, Paulsen KD, Pogue BW and Kanick SC 2016 Wide-field quantitative imaging of tissue microstructure using sub-diffuse spatial frequency domain imaging Optica 3 613–21 [PubMed: 27547790]

McClatchy DM, Zuurbier RA, Wells WA, Paulsen KD and Pogue BW 2018 Micro-computed tomography enables rapid surgical margin assessment during breast conserving surgery (BCS): correlation of whole BCS micro-CT readings to final histopathology Br. J. Res. Treat 172 587–95

Moran MS et al. 2014 Society of surgical oncology-American society for radiation oncology consensus guideline on margins for breast-conserving surgery with whole-breast irradiation in stages I and II invasive breast cancer Int. J. Radiat. Oncol. Biol. Phys 88 553–64 [PubMed: 24521674]

Pluim JPW, Maintz JBA and Viergever MA 2003 Mutual-information-based registration of medical images: a survey IEEE Trans. Med. Imaging 22 986–1004 [PubMed: 12906253]

Papa M et al. 2016 An intraoperative MRI system for margin assessment in breast conserving surgery: initial results from a novel technique J. Surg. Oncol 114 22–6 [PubMed: 27080211]

Park KU, Kuerer HM, Rauch GM, Leung JWT, Sahin AA, Wei W, Li Y and Black DM 2019 Digital breast tomosynthesis for intraoperative margin assessment during breast-conserving surgery Ann. Surg. Oncol 26 1720–8 [PubMed: 30877499]

Partain N, Calvo C, Mokdad A, Colton A, Pouns K, Clifford E, Farr D, Huth J, Wooldridge R and Leitch AM 2020 Differences in re-excision rates for breast-conserving surgery using intraoperative 2D versus 3D tomosynthesis specimen radiograph Ann. Surg. Oncol 27 4767–76 [PubMed: 32740738]

Ridler TW and Calvard S 1978 Picture thresholding using an iterative selection method IEEE Trans. Syst. Man Cybern 8 630–2

Smith T and Guild J 1931 The C.I.E. colorimetric standards and their use Trans. Opt. Soc 33 73–134

Streeter SS, Maloney BW, McClatchy DM, Jermyn M, Pogue BW, Rizzo EJ, Wells WA and Paulsen KD 2019 Structured light imaging for breast-conserving surgery: II. Texture analysis and classification Proc. SPIE 24 096003

Streeter SS, Maloney BW, Pogue BW and Paulsen KD 2020 Active line scan with spatial gating for sub-diffuse reflectance imaging of scatter microtexture Opt. Lett 45 6378–81 [PubMed: 33258816]

Tang R et al. 2016 Intraoperative micro-computed tomography (micro-CT): a novel method for determination of primary tumour dimensions in breast cancer specimens Br. J. Radiol 89 20150581 [PubMed: 26568439]

Tongtong L, Julie MJ, Mollie P, Renee F, Amanda E, Todd D, Taly GS, Dong HY, Tina Y and Bing Y 2020 Rapid assessment of breast tumor margins using deep ultraviolet fluorescence scanning microscopy Proc. SPIE 25 126501

Tse GM, Tan P-H, Pang ALM, Tang APY and Cheung HS 2008 Calcification in breast lesions: pathologists' perspective J. Clin. Pathol 61 145–51 [PubMed: 17704264]

Wang Y et al. 2016 Quantitative molecular phenotyping with topically applied SERS nanoparticles for intraoperative guidance of breast cancer lumpectomy Sci. Rep 6 21242 [PubMed: 26878888]

Wazer DE, DiPetrillo T, Schmidt-Ullrich R, Weld L, Smith TJ, Marchant DJ and Robert NJ 1992 Factors influencing cosmetic outcome and complication risk after conservative surgery and radiotherapy for early-stage breast carcinoma J. Clin. Oncol 10 356–63 [PubMed: 1445509]

Wong TTW, Zhang R, Hai P, Zhang C, Pleitez MA, Aft RL, Novack DV and Wang LV 2017 Fast label-free multilayered histology-like imaging of human breast cancer by photoacoustic microscopy Sci. Adv 3 e1602168 [PubMed: 28560329]

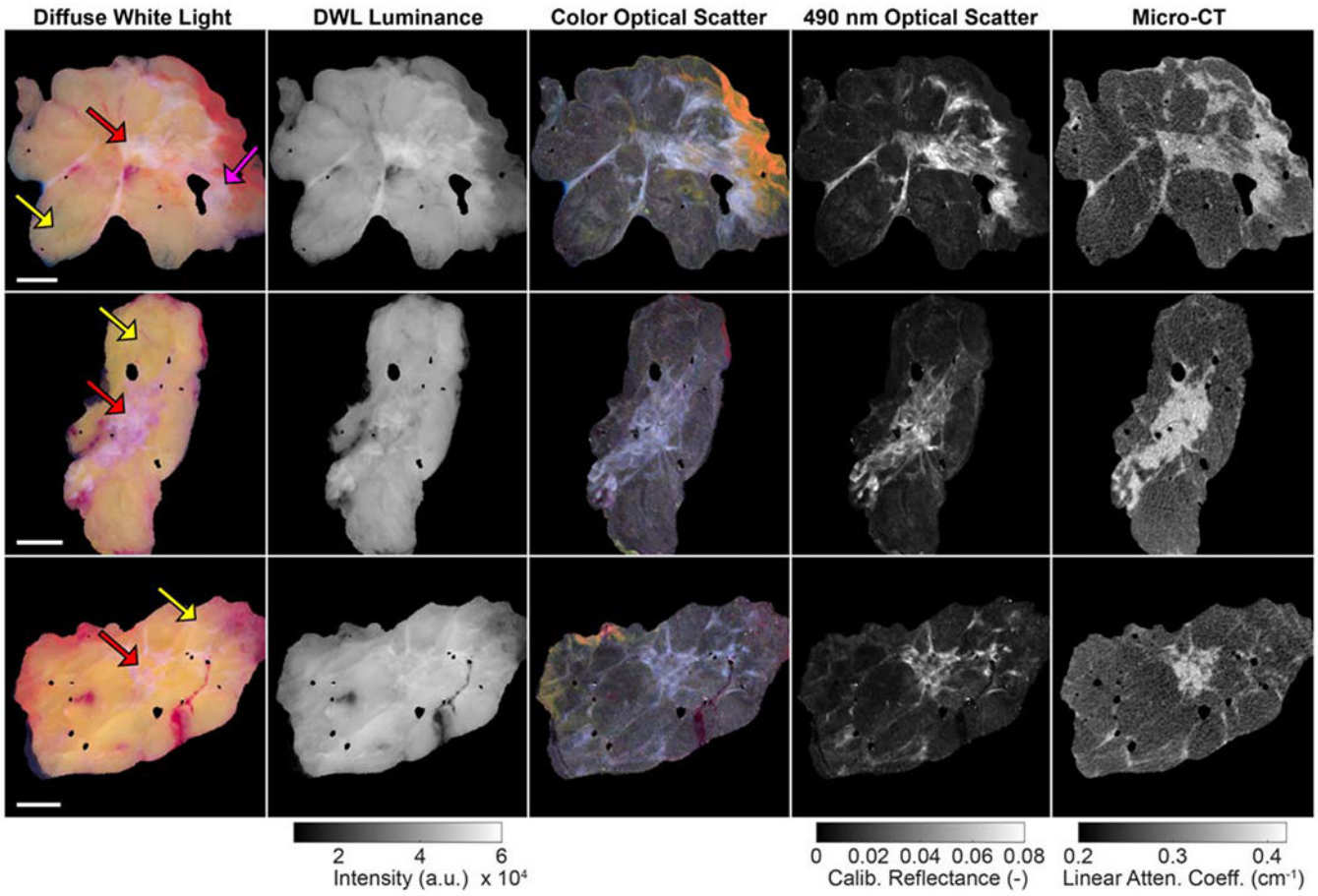

Figure 1.

Wide field-of-view images of representative invasive ductal carcinoma specimens (yellow arrows = adipose tissue; pink arrow = connective tissue; red arrows = malignant tissue). 1 cm scale bars are shown in the first column. In the optical images, surgical ink (yellow, orange, red) is visible along some specimen margins. Linear attenuation coefficient values correspond to 50 kVp. DWL = diffuse white light.

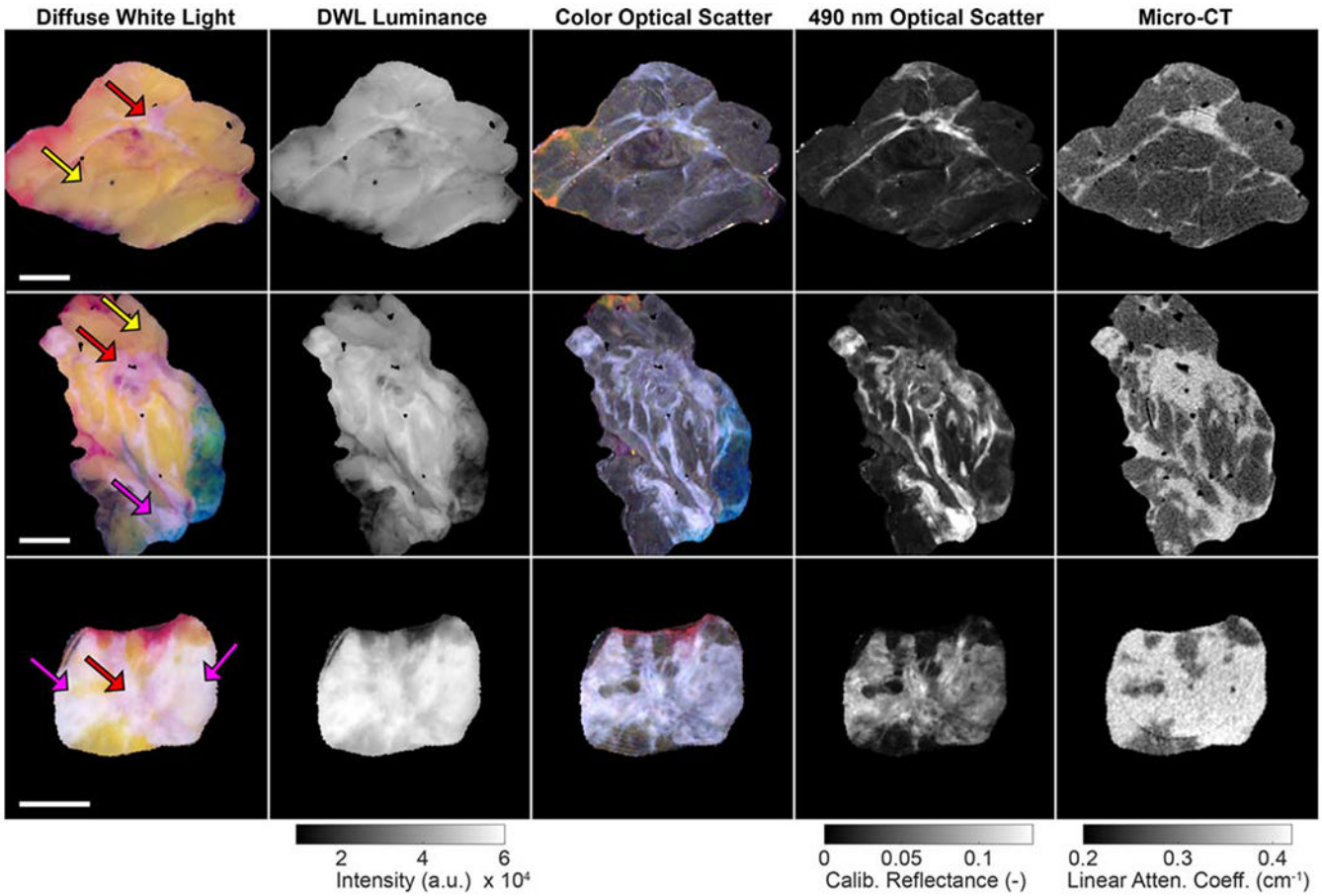

Figure 2.

Wide field-of-view images of representative invasive lobular carcinoma specimens (yellow arrows = adipose tissue; pink arrows = connective tissue; red arrows = malignant tissue). 1 cm scale bars are shown in the first column. In the optical images, surgical ink (orange, red, blue) is visible along some specimen margins. Linear attenuation coefficient values correspond to 50 kVp. DWL = diffuse white light.

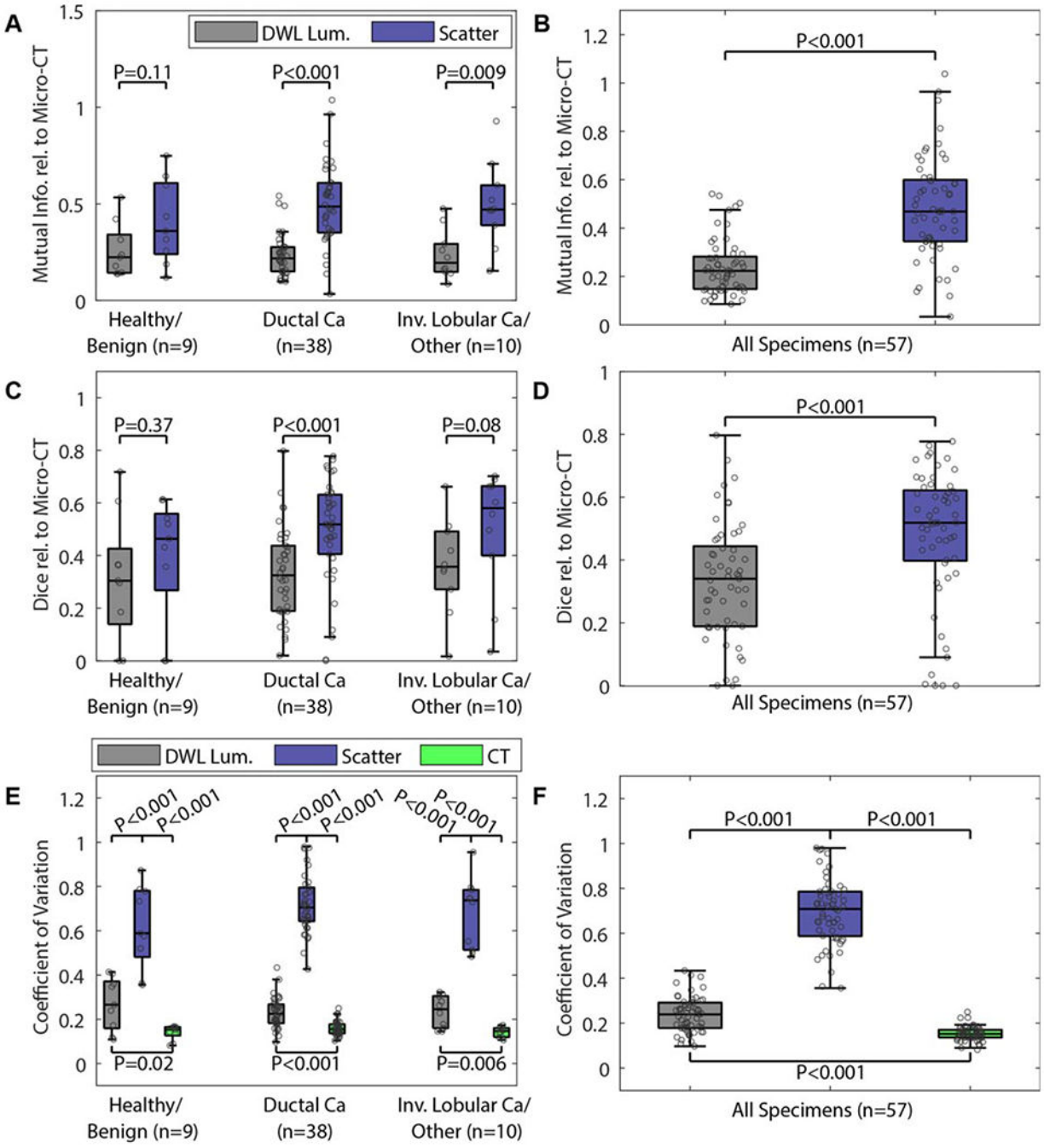

Figure 3.

(A)–(D) Image similarity metrics quantified between micro-CT and either diffuse white light luminance or optical scatter images. (E) and (F) The coefficient of variation quantified for each image type. The legend in (A) applies to all subplots in (A)–(D). The legend in (E) also applies to (F). DWL Lum. = white light diffuse luminance; scatter = 490 nm optical scatter; CT = micro-CT; Ca = carcinoma; other = metaplastic tumor.

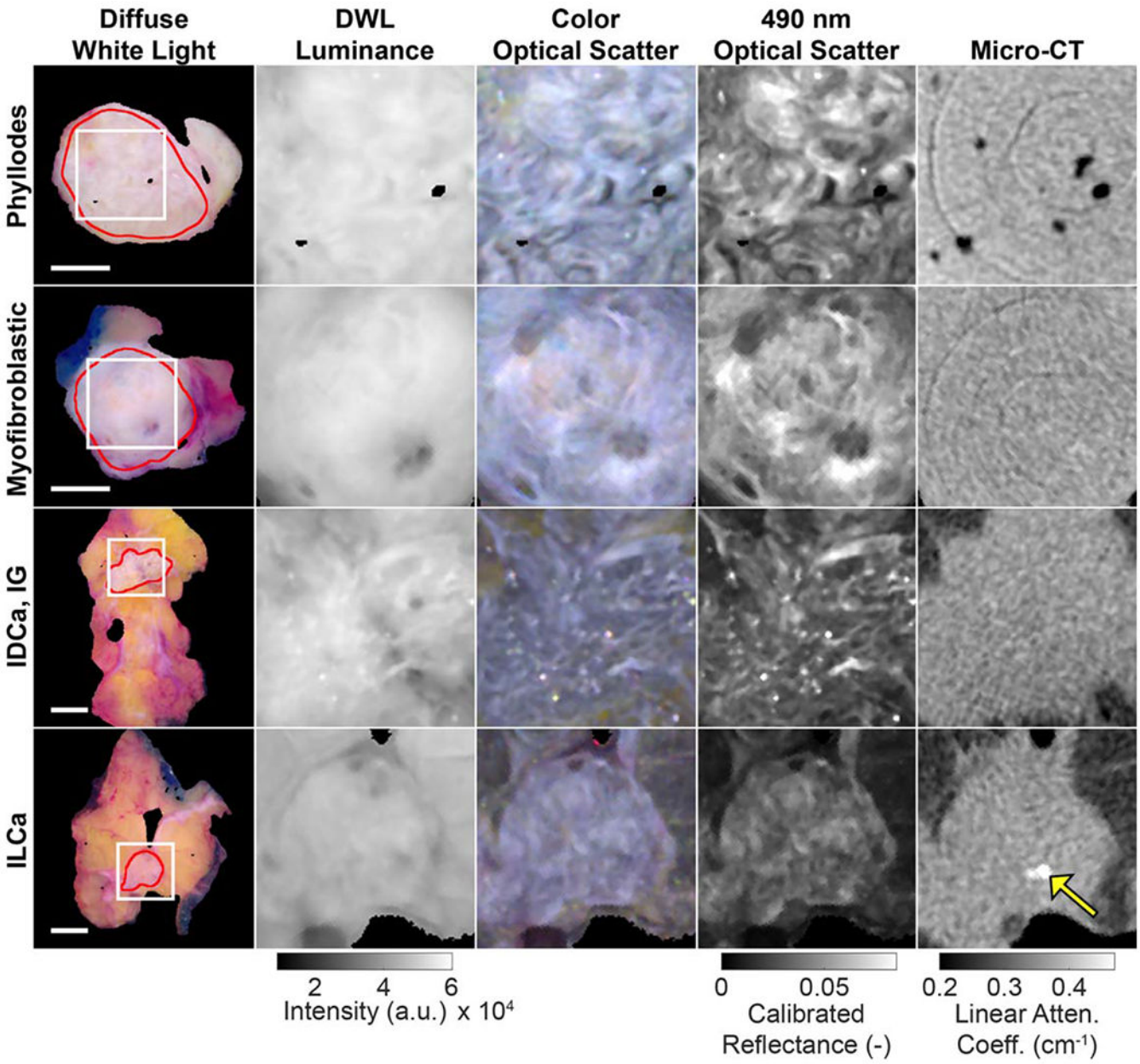

Figure 4.

Representative tumor slices demonstrating intra-tumoral fibrous structures. Regions of interest (white squares, 1.5 cm × 1.5 cm, column 1) magnify the malignant primary tumor (red lines) in the following four columns. Ring artifacts are seen in the micro-CT images in the top two rows, and a microcalcification is seen in the micro-CT of the last specimen (yellow arrow). 1 cm scale bars are shown for each row. Linear attenuation coefficient values correspond to 50 kVp.DWL = diffuse white light; IDCa, IG = invasive ductal carcinoma, intermediate grade; ILCa = invasive lobular carcinoma.

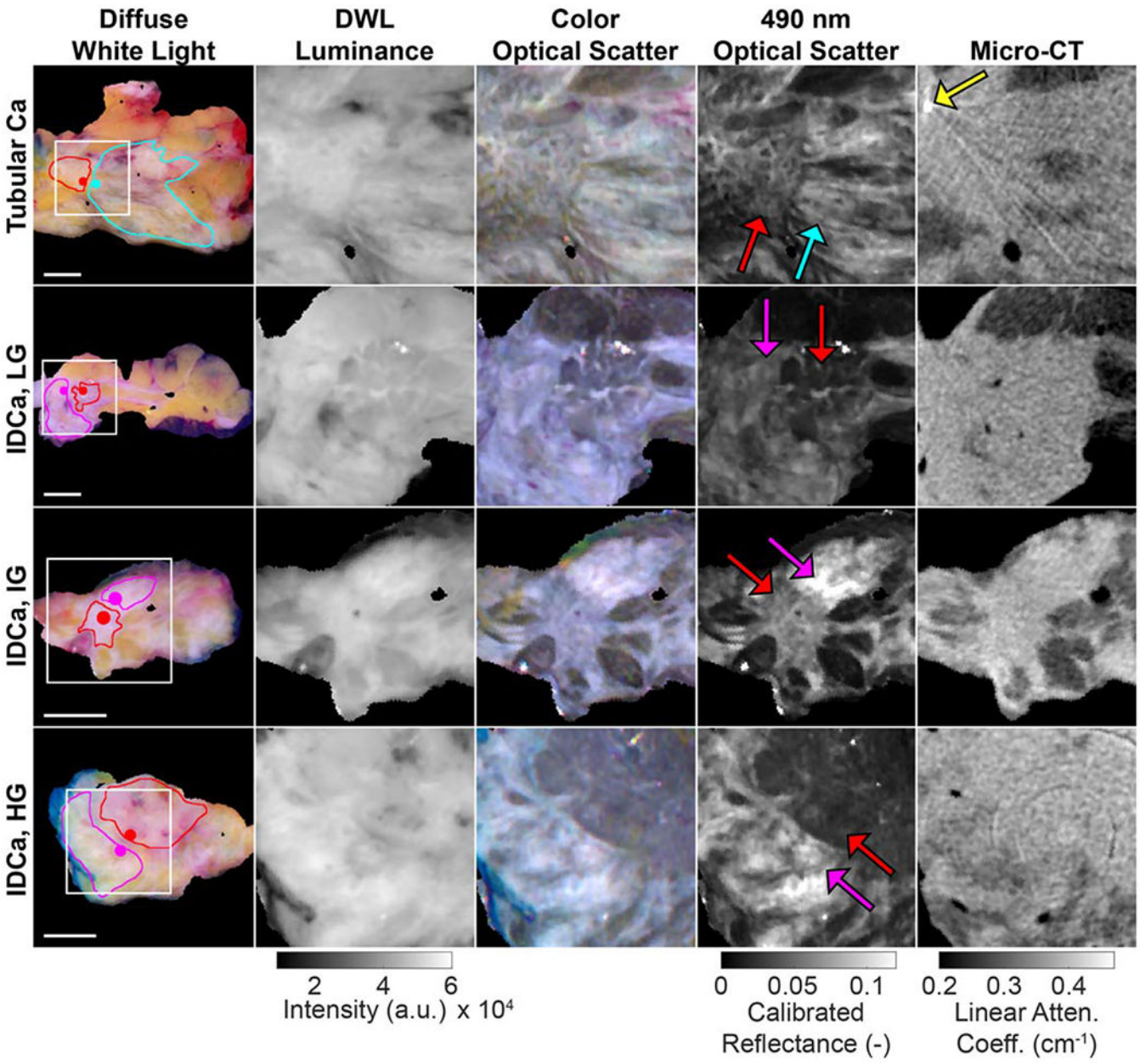

Figure 5.

Representative tumor slices exhibiting malignant tissue boundaries (red lines/arrows) with adjacent non-malignant fibrous tissue (pink lines/arrows = healthy connective tissue; cyan line/arrow = fibrocystic disease). Regions of interest (white squares, 2 cm × 2 cm, column 1) magnify malignant tissue boundaries in the following four columns. A beam hardening artifact from a surgical clip is seen in the top row micro-CT (yellow arrow), and a ring artifact is present in the bottom micro-CT. 1 cm scale bars are shown for each row. Linear attenuation coefficient values correspond to 50 kVp. DWL = diffuse white light; Ca = carcinoma; IDCa, LG = invasive ductal carcinoma, low grade; IDCa, IG = invasive ductal carcinoma, intermediate grade; IDCa, IG = invasive ductal carcinoma, high grade.

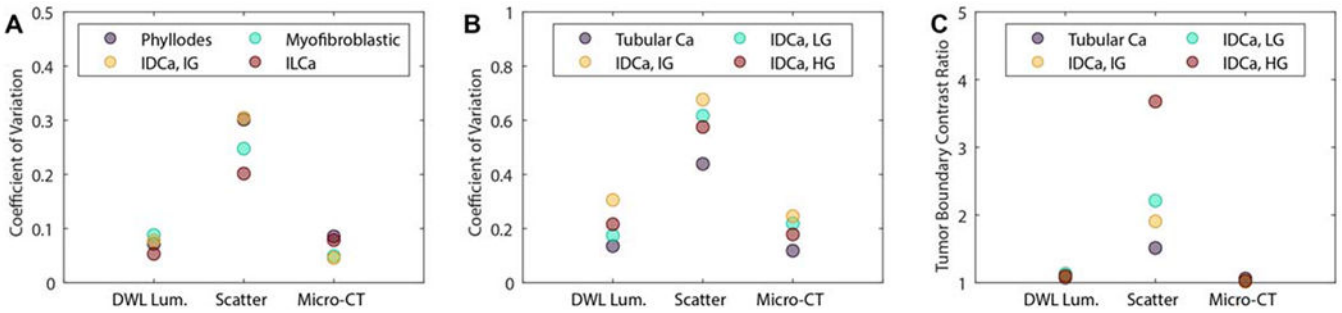

Figure 6.

(A) Intra-tumoral structure CV values from 1.5 cm × 1.5 cm tumor-bearing ROIs shown in figure 4. (B) Tumor boundary CV values from 2.0 cm × 2.0 cm ROIs shown in figure 5. (C) TBCR values quantified in 2 mm diameter samples on either side of the tissue boundary (solid colored dots in figure 5 column 1).DWL Lum. = diffuse white light luminance; scatter = 490 nm optical scatter; Ca = carcinoma; IDCa, LG = invasive ductal carcinoma, low grade; IDCa, IG = invasive ductal carcinoma, intermediate grade; IDCa, IG = invasive ductal carcinoma, high grade; ILCa = invasive lobular carcinoma.

Table 1.

Summary of imaged breast-conserving surgery specimens by primary tissue subtype. Inv = invasive.

Primary diagnosis	Specimen count
Healthy and benign	
Healthy connective tissue[a]	3
Fibrocystic disease	1
Fibroadenoma	3
Myofibroblastic	1
Phyllodes	1
Subtotal:	9
Pre-invasive and invasive ductal carcinoma Ductal carcinoma *in situ*	3
Inv. tubular carcinoma	2
Inv. ductal carcinoma low grade	9
Inv. ductal carcinoma intermediate grade	14
Inv. ductal carcinoma high grade	8
Inv. mucinous carcinoma	2
Subtotal:	38
Invasive lobular carcinoma/Other	
Inv. lobular carcinoma	9
Inv. metaplastic	1
Subtotal:	10
Total:	57

[a]The imaged surface of these specimens did not contain abnormal benign and/or malignant lesion(s) based on histological analysis.